Spatial Confinement of Electromagnetic Hot and Cold Spots in Gold Nanocubes

Mohamed Haggui,[†] Montacer Dridi,[‡] Jérôme Plain,[†] Sylvie Marguet,[§] Henri Perez,[§] George C. Schatz,[‡] Gary P. Wiederrecht,[⊥] Stephen K. Gray,[⊥] and Renaud Bachelot[†,*]

[†]Laboratoire de Nanotechnologie et d'Instrumentation Optique LNIO—CNRS UMR 6279, Université de Technologie de Troyes, Troyes, France, [‡]Department of Chemistry, Northwestern University, Evanston, Illinois 60208, United States , [§]CNRS-CEA, IRAMIS, SPAM, Laboratoire Francis Perrin, URA2453, 91191 Gif-sur-Yvette, France, and [⊥]Center for Nanoscale Materials, Argonne National Laboratory, Argonne, Illinois 60439, United States

ABSTRACT

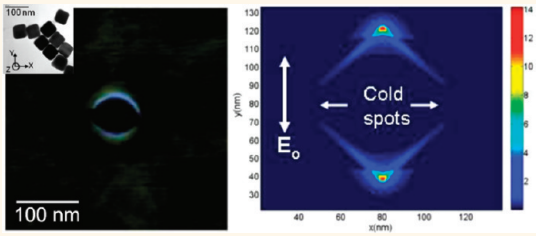

We report a near-field imaging study of colloidal gold nanocubes. This is accomplished through a photochemical imaging method in which molecular displacements are vectorial in nature, enabling sensitivity to the polarization of the optical near-field of the nanocubes. We analyze the confinement of both electromagnetic hot and "cold" spots with a resolution of $\lambda/35$ and emphasize the particularly high spatial confinement of cold spots. The concept of a cold spot complements the well-known electromagnetic hot spot but can have significant advantages. The application of the ultraconfined cold spots to high resolution imaging and spectroscopy is discussed.

KEYWORDS: plasmon · gold · nanocubes · photoisomerization · near-field photochemical imaging · near-field depolarization · azobenzene · electromagnetic hot spot · electromagnetic cold spots

Over the past decade the optical properties of metal nanoparticles[1,2] have been the subject of increasing research efforts that are motivated by potential applications in many areas, including chemical/biological sensing,[3−6] energy harvesting,[7] light generation,[8] data storage,[9] near-field imaging,[10,11] and nanoscale photochemistry.[12] This area of research, generally denoted as "plasmonics", has derived clear benefits from intensive improvements in electromagnetic modeling,[13] characterization methods,[14−19] and nanofabrication.[20] Regarding this last point, various bottom-up[21−23] and top-down[24−32] approaches of fabrication have enabled the study of metal nanostructures of complex geometries. Among them, metal nanocubes have been of recent interest. Studies on the optical properties of nanocubes have so far dealt with local light enhancement for the purpose, for example, of maximizing signal from analytes using surface-enhanced raman scattering (SERS),[33] cell imaging, and photothermal therapy of human liver cancer cells[34] and enhancing fluorescence and photovoltaic yield.[35] Other recent studies on single silver nanocubes, in interaction with a nearby dielectric substrate, show that this type of nanostructure may play an important role as a localized surface plasmon resonance sensor with high performance sensitivity.[36,37]

Nanocubes have particularly interesting plasmonic properties. In particular, a given cube presents 12 sharp ridges and 8 corners, leading to a complex multipolar resonance structure. Silver cubes are very sensitive to corner and edge rounding.[36−38] Gold Nanocubes show less significant resonance structure than silver cubes due to quenching of the higher multipole resonances by interband transitions.[39] However, even for rounded cubes made using wet chemistry methods, there can be strong contrast in light confinement for small changes in wavelength which can be of great interest for plasmonics.

In this letter, for the first time to our knowledge, we investigate optical near-field confinement near single gold nanocubes through a unique and recently introduced approach of photochemical near-field imaging, where photoinduced molecular displacements are analyzed as a vectorial signature of the optical near-field.[40,41] We also introduce a point of view that is complementary to those considered so far: we monitor the confinement of both the

* Address correspondence to renaud.bachelot@utt.fr.

Received for review October 20, 2011 and accepted January 26, 2012.

Published online January 26, 2012
10.1021/nn2040389

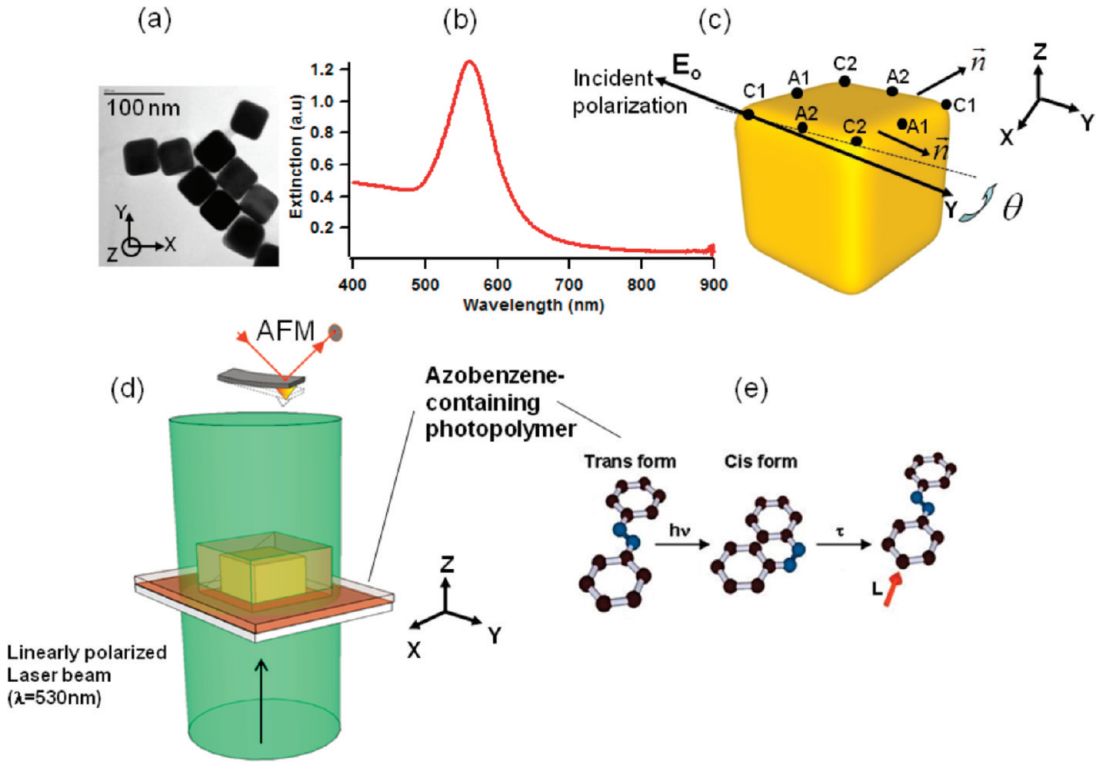

Figure 1. The gold nanocube sample and principle of the near-field photochemical imaging method are illustrated. (a) TEM image of 60 nm gold nanocubes (GNCs); (b) extinction spectrum of the GNCs in water; (c) representation of GNC geometry, points of interest and incident polarization; (d) principle of the experiment (see text for details); (e) illustration of a cycle of photoisomerization (trans→cis→trans) and the resulting molecular displacement.

enhanced light and the *absence* of light. We call a region of confined absence of light a "cold spot", which is in contrast to the well-known "hot spot" concept.[42] While strictly not an application of the Babinet principle[43] [see Supporting Information (SI)], the idea of complementary cold spots to hot spots is in the spirit of this principle. We present an experimental description of field localization on the nanocube surface at a sub-15 nm scale and show that cold spots can be more spatially confined than hot spots on the cube surface.

PHOTOCHEMICAL APPROACH

Gold nanocubes (GNCs) were prepared by colloidal chemistry following a two-step "seed-mediated" approach (see Methods for details).[44] In the past few years, this approach has been used to synthesize a spectacular variety of shapes such as spheres, rods, wires, cubes, triangular nanoprisms, bipyramids, and stars.[45] Figure 1 displays the resulting nanocubes, as well as the photochemical approach. Figure 1a and Figure 1b show, respectively, a TEM image of the synthesized 60(±3)-nm-side GNCs and corresponding absorption spectrum in water, as measured by extinction spectroscopy. Figure 1b shows a clear dipolar plasmon resonance at λ = 560 nm. It is believed to correspond to the average contribution of the 12 identical ridges excited by randomly polarized white light. The different zones of interest, localized at the GNC surface, are represented in Figure 1c. We will come back to this figure in the following.

The ``photochemical imaging'' of optical near-fields of the GNCs is based on the use of azobenzene-containing photosensitive polymers.[40,46−48] GNCs are coated with a thin layer of this photopolymer and subsequently laser-illuminated (see Figure 1d). The azo molecules act as tiny optical probes undergoing under optical excitation, cycles of isomerization, and subsequent nanodisplacements (see Figure 1e) inducing topographical changes that are characterized by atomic force microscopy.

The origin of this topography has been extensively discussed elsewhere.[40,41,46−49] Important aspects will be reiterated here in the context of the present study. The incident polarization state is linear and parallel to the *Y*-axis and is kept constant. Any studied single cube is characterized by θ, which is the in-plane angle between the incident field direction and the cube left side relative to the center of the cube top face when viewed along the *Y*-direction (see Figure 1c). For any specific location at the top of the cube, the local excited polarization charge density strongly depends on θ in terms of the component of the incident field along local normal unit vectors $\vec{n}$ represented in Figure 1c. In nanocubes, the spatial distribution of induced charge can change dramatically from one cube to the next due

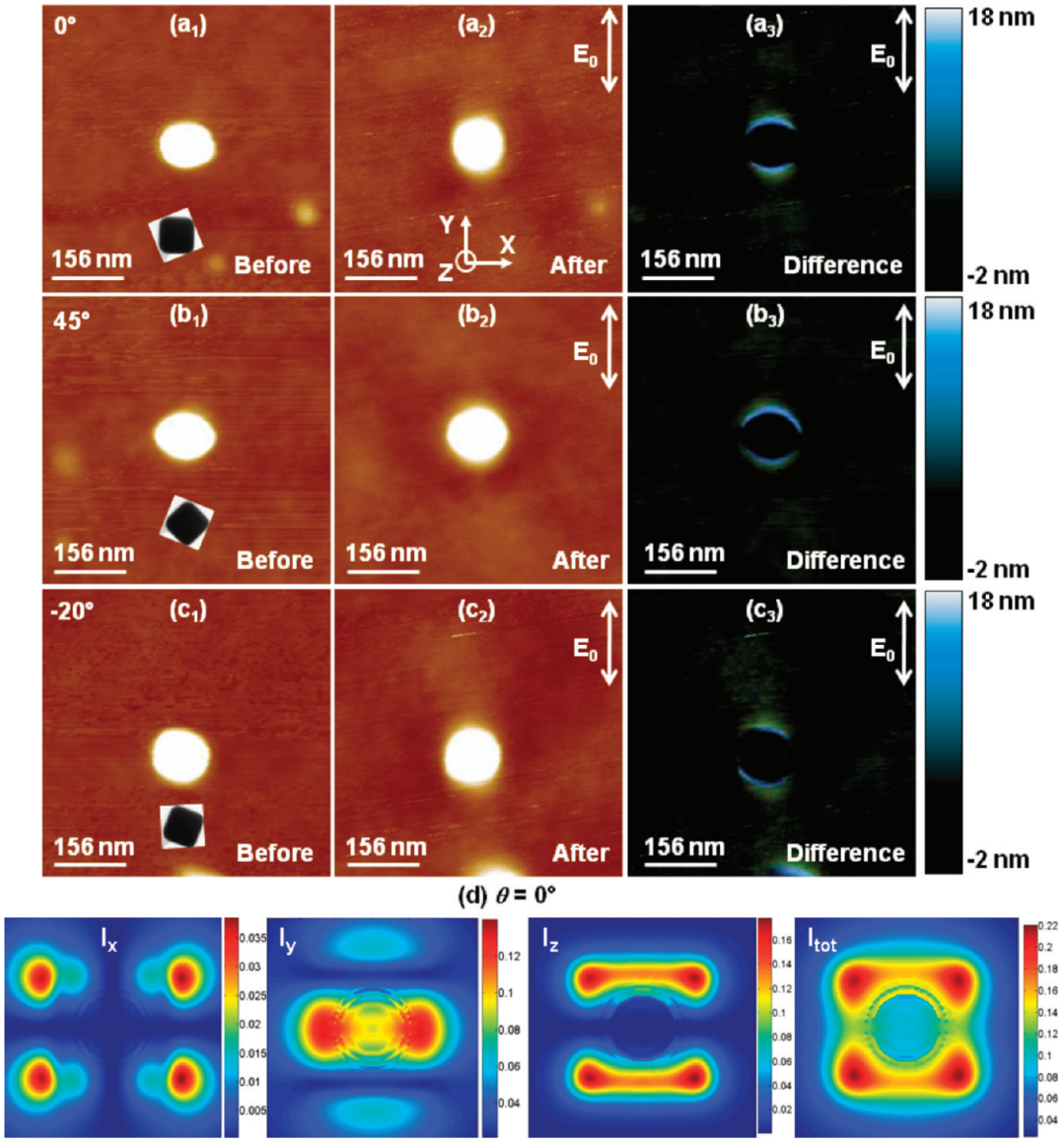

Figure 2. Photochemical imaging of the optical near-field of a single GNC illuminated by a *Z* propagating plane wave linearly polarized along *Y* ($\lambda = 530$ nm). (a_1, b_1, c_1) AFM images of PMMA-DR1 covered GNCs with different orientations relative to the *Y* direction: $\theta = 0°$, 45°, −20°, respectively. θ is determined through phase imaging (see Supporting Information). These images were recorded after polymer deposition, before optical exposure. Corresponding TEM images are also shown in insets. (a_2,b_2, c_2) AFM images of the same GNCs as for images a_1, b_1, and c_1 taken after a 5-min exposure. (a_3,b_3,c_3) Differential AFM images (column 2 − column 1), highlighting the optically induced topography in the vicinity of the GNCs. Color code: bright corresponds to matter accumulation and black indicates no surface deformations. (d) FDTD calculation of the intensity of the different field components *X*, *Y*, *Z* and total (140 × 140 nm^2 maps). Rounded cubes (radius of curvature = 8 nm) deposited on ITO substrate are considered, and edge length is 63 nm. The plane of observation is 10 nm distant from the cube top surface. In general the apparent cube size and shape in images a_1, b_1, and c_1 result from both AFM resolution and thickness/geometry of the polymer deposited onto the cubes (see Supporting Information, Figure S2 as an illustration).

to the specific geometry of each cube. In particular, the charge can go to zero at very confined localizations.

RESULTS AND DISCUSSION

To introduce the analysis, a first set of results is shown in Figure 2. Figures $2a_1$ and $2a_2$ show AFM images of a single GNC taken, respectively, before and after exposure in the $\theta = 0°$ case. The orientation of the GNC is represented by the TEM image in Figure $2a_1$. In general, to make sure that the evaluated value of θ is correct, extra AFM analyses were performed. They include phase imaging and use of very sharp tips (tip radius of curvature < 10 nm). More detailed information about this point can be found in the Supporting Information (Figure S1). Figure $2a_3$ is the differential image obtained by subtracting image $2a_1$ from image $2a_2$. It highlights the optically induced molecular displacement regardless of the initial topography. Figure $2a_3$ show a clear contact along the ridge [C1A1C2] that is represented in Figure 1c, while the ridge [C1A2C2] remains dark. The interpretation of the observed contrast relies on both our knowledge of

PMMA-DR1 and the electromagnetic calculations shown in Figure 2d. The calculations are based on the finite-difference time-domain (FDTD) method which is widely utilized to numerically simulate the propagation and localization of electromagnetic waves (see SI for details).[13] All of the experimental parameters have been taken into account in the FDTD calculations: the presence of the substrate, incident wavelength, thickness of the polymer, roundness of cube corners, *etc*. Figure 2d shows the intensity map of different field components at a 10 nm distance from the top surface of a GNC that is illuminated with a *Y* polarized plane wave, in the $\theta = 0°$ case. The most intense regions near the corners are due to the lightening rod effect and there are interesting depolarization effects that we will return to later. Furthermore, rounding effects due to the lossy character of gold, are not especially strong. It is thus expected that this effect has a secondary role in the photoinduced topography, though it is not null. From Figure 2d, it is apparent that the light undergoes strong depolarization in the close vicinity of the cube: the *Y*→*Z* polarization transition is strong and the resulting intensity is about 3 times higher than the intensity of the local field component along the incident *Y* polarization direction. The *Y*→*X* transition (left image) is present also, although weaker than *Y*→*Z*. The two right images of Figure 2d show that the total intensity is dominated by the *Z* polarized field.

We argue that this longitudinal *Z* component is at the origin of the observed contrast in Figure $2a_3$. This hypothesis is based on what has been learned about the local optical response of PMMA-DR1 over the past few years. In particular, it has been shown that the optically induced topography process is very sensitive to longitudinal fields: even weak fields oriented perpendicular to the polymer surface lead to high (positive) topography while lateral fields are much less efficient in making matter move from bright zones to dark zones, leading to a negative topography contrast corresponding roughly to the inverse of the intensity of the lateral field component.[40,41,46−49] As a result, in the presence of any (even weak) longitudinal field, the topography is expected to represent the positive photography of the *Z* intensity, explaining what is observed in Figure $2a_3$: two high-topography wings along the cube edges that are perpendicular to the incident polarization, comparable to the I_z image of Figure 2d.

However, some differences between Figure $2a_3$ and the calculated I_z map (Figure 2d) are noticeable. The calculated I_z map shows four zones where the intensity looks higher, corresponding to a weak lightning rod effect at the rounded corners. In Figure $2a_3$ these 4 zones of extra-intensity are not visible. This difference is believed to result from the effective distance of observation that lowers the resolution. Figure 2d shows Intensity maps at a 10 nm distance from the

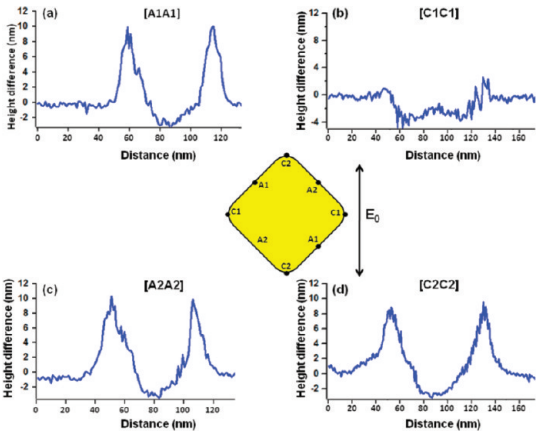

Figure 3. Typical differential AFM profiles along the different directions depicted in the inset (which is a top view of Figure 1c for $\theta = 45°$).

cube top surface. We choose this distance because it corresponds to the polymer thickness. At this distance, the 4 hot spots are poorly contrasted and the calculated image appears very similar to the experimental image. In particular, at this 10-nm distance, the contrast between corner intensity and edge intensity is about 20% (0.18 *vs* 0.14). Additionally, the precision we have on the polymer thickness is about ±3 nm. That means that this effective experimental distance can reach 13 nm, leading to an additional smoothing in the recorded I_z map. Finally, the difference between Figure $2a_3$ and Figure 2d can be explained by an anomaly in polymer response. This anomaly will be introduced and discussed in detail later.

The spatial distribution of the local intensity can be understood on the basis of efficiency of surface charge excitation. We propose that the local molecular displacement is driven by the local optical field resulting from excited surface charges. These charges are related to the electric field discontinuity at the metal-dielectric interface following the usual boundary conditions:

$$E_{1n} - E_{2n} = \rho_{s,\mathrm{pol}}/\varepsilon_0 = \chi \vec{n} \cdot \vec{E}_0 \qquad (1)$$

where E_{1n} and E_{2n} are the normal components of the electric field inside and outside of the GNC, respectively, E_0 is the incident electric field, $\rho_{s,\mathrm{pol}}$ is the surface density of polarization charges (no external charges are considered), and χ is the metal electric susceptibility. In turn, the excited surface charges create their own electric field whose *Z* component is responsible for subsequent mass transport in PMMA-DR1. In particular, in Figure $2a_3$, high topography is observed along the cube ridges where $\vec{n}$ is parallel to E_0 while dark (cold) zones correspond to cube ridges where $\vec{n}$ is perpendicular to E_0. Along such an edge, no charge density is excited and no molecular motion is triggered. In the case of $\theta = 0°$, the dark zone is as large as the bright zone. The situation is different for $\theta = 45°$ (Figure $2b_1$, $2b_2$, $2b_3$).

In this case, the zone where $\vec{n}$ is perpendicular to E_0 is extremely localized to points near C1 (see Figure 3) leading to a cold spot whose apparent size is less than 10 nm as measured by atomic force microscopy (Figure 2b$_3$). On the other hand, at any localization other than C1, E_0 has a nonzero component along $\vec{n}$ and charges are induced with a maximum at C2 where $\vec{n} \| E_0$. This point is of importance and, as far as we know, addressed here for the first time: corners of metal nanocubes can support highly localized cold spots where the local electromagnetic activity is null. Obviously, the total field experienced by the nanostructure is the vectorial sum of incident field (E_0) and local field (E_{loc}). Thus, even at a cold-spot, the *E*-field intensity is not null. However, $E_{loc} > E_0$ far from cold-spots.

In principle, unlike hot spots, cold spots could have point-like features (a "dark dipole"). Compared to a dipole, a "dark dipole" can be defined as a very confined area around a metal nanostructure characterized by a local field equal to zero (and thus no polarization charge excitation and no extra-light radiation). In Figure 2b$_3$, the apparent spatial extension is due to the corner geometry, AFM resolution, polymer thickness, and spatial resolution of the photopolymer. In the case of intermediate values of θ (*e.g.*, $-20°$, see Figure 2c$_1$, 2c$_2$, 2c$_3$), the cold spots are less confined.

In Figures 3 and 4 we go deeper into the analysis. Figure 3 shows differential typical profiles, taken from one GNC characterized by $\theta = 45°$, along four important directions (illustrated in Figure 1c) at the top surface of the GNC: two perpendicular bisectors ([A2A2], [A1A1]) and two diagonals ([C1C1] and [C2C2]). For clarity, in the centered inset, a top view of the cube is shown for the $\theta = 45°$ case.

These profiles indicate that the electromagnetic intensity (observed through mass transport) is characterized with a resolution of about 15 nm ($\sim\lambda/35$) and is localized very close to the 60 nm size cube. In other words, an optical near-field contrast is here observed. We believe that the thickness of the deposited polymer ($\sim$10 nm) is a crucial parameter: the far field background is filtered out and only the very-near field was selected. Figure 3 shows that the only inactive (in the electromagnetic sense) direction is [C1C1] which is perpendicular to the incident polarization. All other directions are excited and show a nonzero electromagnetic near-field. The cases [A1A1] and [A2A2] are similar to each other because they are symmetrical with regards to E_0. They present two peaks that are symmetrically displaced relative to the $\sim$60 nm scan point. These peaks occur when the AFM tip is near edges. The width of the peaks is a signature of the spatial extension of the electromagnetic effect. The spatial extension here is small (fwhm $\approx$ 10 nm) because the electromagnetic edge effect is very confined and spatially selective along the perpendicular bisectors.

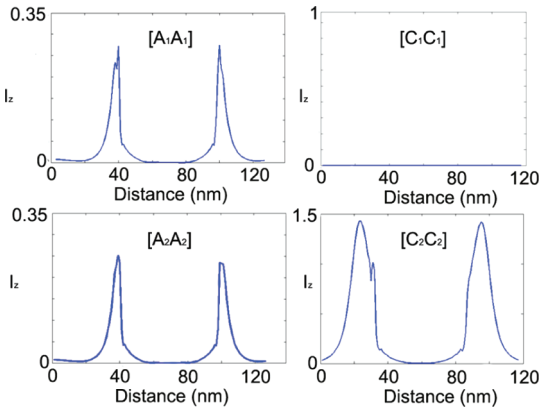

Figure 4. Calculated I_z profiles along the different directions depicted in the inset of Figure 3, for $\theta = 45°$.

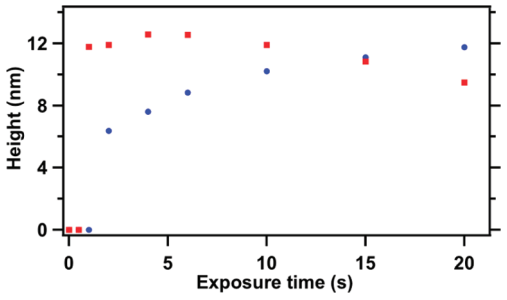

Figure 5. Time evolution of height topography at corner C2 (red squares) and edge A1 (blue circles) for the 20 first seconds of exposure ($\theta = 45°$).

Along the [C2C2] diagonal, two peaks separated by $\sim$100 nm are observed. Their fwhm is significantly bigger than for [A1A1] and [A2A2]. This is likely to result from a weak lightning rod effect that occurred at the corner, increasing the effective depth of the locally enhanced field. However, the height was expected to be higher for the polarization aligned with the direction [C2C2] where the lighting rod effect can be excited at the corner. This expectation is supported by numerical profiles, calculated for $\theta = 45°$, and illustrated in Figure 4, where both the fwhm and height are at a maximum at C2. Surprisingly, compared to [A1A1] and [A2A2] the apparent measured height at [C2C2] is comparable, or even weaker in Figure 3. This phenomenon is supposed to result from the specific material response, especially its time evolution. To make clear this point, we carried out a study of the time evolution of the measured height. This study is presented in figure 5 which shows the topography at C2 and A1 for the 20 first seconds of exposure. At each time, the exposure was stopped and AFM measurements were performed. Figure 5 shows that, at short times, the topography at C2 quickly reaches a maximum which is much higher than the topography at A1, as expected from Figure 4. Afterward, the C2 topography decreases. This phenomenon is typical to local high intensity hot spots; it results from polymer growth saturation and

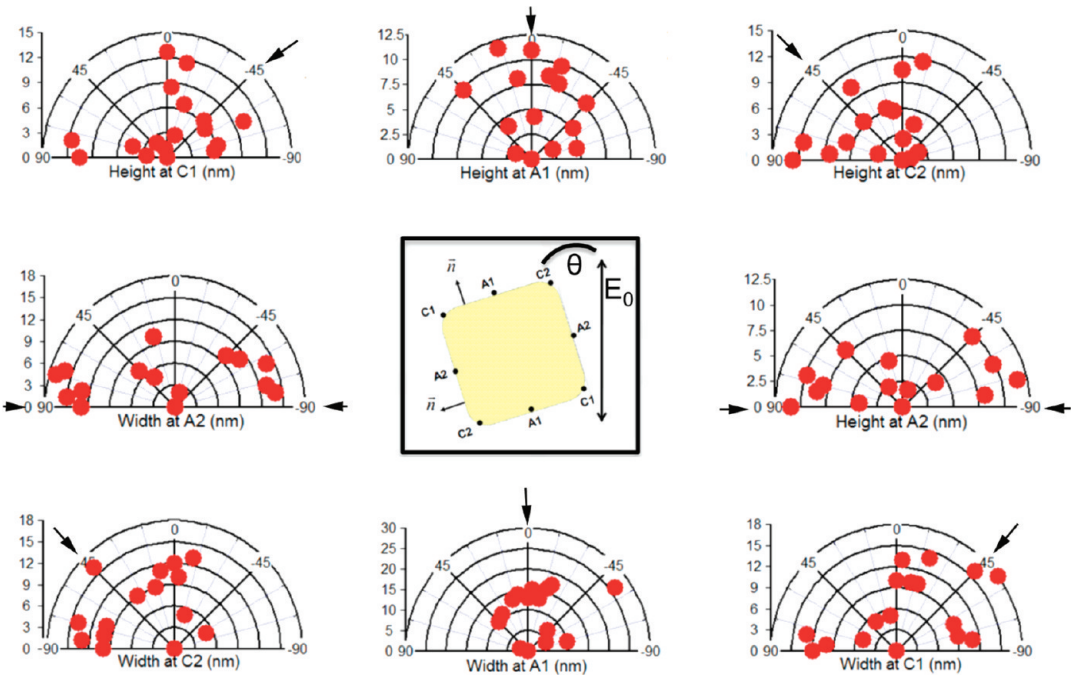

Figure 6. Polar diagrams showing height and width (see text for definition of these terms) of the optically induced topography, at different points on the GNC top surface, as a function of θ (the nanocube orientation). The location of these points is represented in the centered figure which is a top view of Figure 1c. Dot diameter represents experimental error bars. The black arrows in the diagrams point out "active" angles (middle of the envelopes).

time polymer relaxation as reported in ref 47. On the other hand, the time evolution of the topography at A1 is smoother: it slowly increases because the associated intensity is weaker.

As a result, polymer heights measured after 5 min (Figures 2 and 3) are believed to correspond to postsaturation values and are not ideally proportional to local field intensities. This anomaly, for the moment, limits precise quantification of the electromagnetic enhancement. Further experiments will be performed in the near future. In particular systematic time evolution studies will be carried out at different GNP positions, time scales, and intensity ranges, with the goal of quantifying material response and involved intensities at the nanoscale. Despite this anomaly, as it will be shown in the following, under the current experimental conditions, we were able to define electromagnetic activity at specific areas of the GNC surface.

Figure 3 therefore highlights the fact that local optical fields and sources can be either activated or turned off, on demand, at the surface of a metal nanocube, by controlling the incident polarization relative to the spatial orientation of the cube.

Figure 6 shows polar diagrams that were generated to provide a complete analysis. For each major position at the top cube surface, the width and height of bright contrast (hot spots) have been measured, from AFM differential profiles, as a function of θ. Again, for readability, a top-view of Figure 1c is shown in Figure 6. Fourteen differently oriented GNCs were analyzed. As explained earlier, the "width" is defined as the fwhm of the peaks of the differential AFM profiles along axes linking the center of the C2C1C2C1 square and the points of interest. This width is the signature of the spatial field confinement in a direction which is radial to the cube (in a planar direction that passes through the center of the cube), while "height" reflects the relative level of the intensity of the relevant Z field component.

The C1 case is generally characterized by an envelope centered at $\theta = -45°$ (or 315°), in accordance with the fact that this tip corner is efficiently excited when parallel to the incident field. On the other hand, around $\theta = +45°$, the envelope tends to sink down: a cold spot is progressively replacing a hot spot. As expected, the C2 case is symmetrical to the C1 case: the excitation of this corner is maximized around $\theta = +45°$ and tends to vanish when θ converges to $-90°$ (270°) where the incident field is perpendicular to the local normal unit vector at C2. As far as A1 is concerned, the electromagnetic excitation is maximum around 0° for which the incident field efficiently induces charge density at the [C1A1C2] edge. By contrast, a minimum is observed, at this angle, along the [C1A2C2] edge, because the incident field is tangential to the [C1A2C2] edge and no charge is induced. The A2 case is indeed complementary to the A1 case: excitation of the edge is efficient around $\theta = \pm 90°$ for which the component of incident field along the normal unit vector is large.

Interestingly, in all diagrams, it is noticed that the angles for which the "width" presents a maximum does not necessarily correspond to a maximum in the

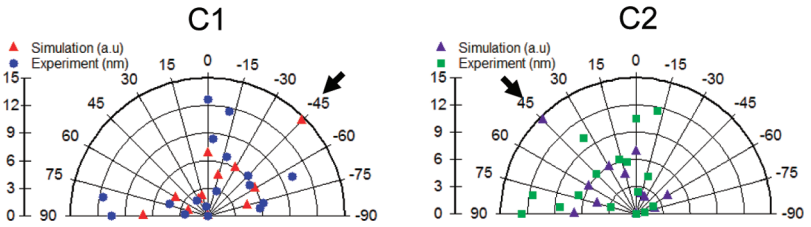

Figure 7. Polar diagrams showing experimental height of the optically induced topography (rounded dots) and calculated I_z (triangles) as a function of θ. Data are taken at two points on the GNC top surface: C1 (left) and C2 (right). Anomalies at $\pm 45°$ are clearly visible. They are pointed out by thick black arrows.

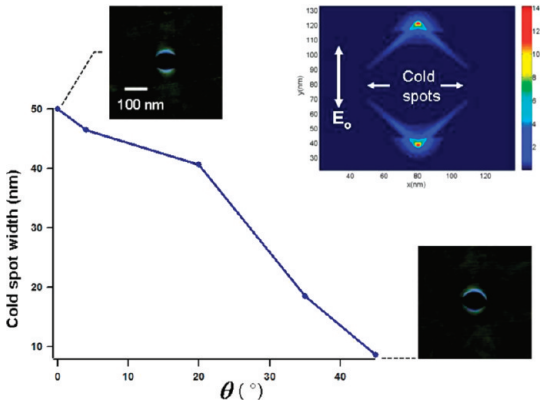

Figure 8. Lateral size, as measured though our approach, of the cold spots along the GNC edges as a function of cube orientation θ. Differential AFM images are shown for the two extreme cases: $\theta = 0°$ and $\theta = 45°$. Top right: FDTD calculation illustrating a cold spot in the case of 45° incident polarization (I_z map at 3 nm height above the cube).

"height" diagram. This is likely to be due to the anomaly (commented in detail with Figure 3) in longitudinal polymer response for the highest intensities. Figure 6 constitutes a valuable mapping of the local optical near-field at the top side of the GNC even though, as explained in earlier sections, ideal quantitative analysis is for the moment not possible due to this anomaly in polymer response. As a result, some pattern changes look abrupt in Figure 6. These changes do not reflect the exact level of the local intensity. The most important point emphasized in Figure 6 is that we are able to define *envelopes*, centered at specific positions. These envelopes allow us, for the first time to our knowledge, to localize near-field electromagnetic activity as a function of the cube orientation. This capability is supported by Figure 7 which shows comparisons between experimental and numerical polar diagrams at C1 and C2 GNC localization. The agreement between the two diagrams is pretty good in the sense that the general envelopes fit well, despite the anomaly clearly visible at $\theta = +45°$ for C2 and $-45°$ for C1, that is, where light is strongly enhanced through the lightning rod effect excited at the corners.

As pointed out before and illustrated in Figure 3, along the cube edges, hot spot confinement is limited by the fact that the parts of the edges where the incident field has a nonzero component along the local normal are widespread and not isolated. On the contrary, a cold spot can be much more confined because isolated points where the scalar product in eq 1 goes to zero can be found. (Another reason for the greater confined character of a cold spot is that it can be associated with lower dimensional nodes in the electromagnetic field components.)

This point of view is clearly illustrated by Figure 8, which shows the variation of the cold zone lateral size as a function of θ. This size is defined as the length of uninterrupted black zone (null signal in the differential AFM image) along the [C1A2C2A1C1] half perimeter at the GNC top surface. The cold spot width dramatically drops from 50 to 10 nm as θ varied from 0 to 45°. This shows that manipulating the cube orientation, with respect to the incident polarization direction, allows us to control the spatial dimension of the cold spot. Hence, we can obtain confined cold zones (as that illustrated in FDTD map shown at the top right of Figure 8) in well-defined locations and with well-defined dimensions.

We suggest that such cold spots could be exploited in nanoscale fluorescence. A cold spot, in contact with a fluorescent particle to be studied, would be alternatively activated with a time varying polarization direction. The resulting fluorescence would be detected by lock-in detection at the frequency of polarization modulation. The approach proposed here is reminiscent of the first ideas of "apertureless" scanning near-field optical microscopy where a metal tip was found to locally turn off a diffraction spot.[50] This method could minimize bleaching effects and optimize spatial resolution which would be associated with cold spot confinement.

CONCLUSION

The optical field at the top surface of gold nanocubes was analyzed with a $\lambda/35$ resolution through an imaging approach based on the use of azoic molecular probes. It is shown that our approach enables experimental determination of local electromagnetic activity at different cube areas as a function of cube orientation.

The concept of plasmonic "cold spot" was introduced as well. It corresponds to a localized absence of

charge excitation at the surface of the metal nanostructures. Cold spots were detected *via* an absence of molecular photodisplacement. Both hot spots and cold spots were investigated as a function of nanocube orientation relative to the incident field direction. We find that cold spots are more confined than are hot spots along the nanocube edges. This feature could be exploited for improving spatial resolution in near-field optical microscopy and spectroscopy.

METHODS

Gold Nanocubes Synthesis. Nanocubes of edge length 60 ± 3 nm were prepared following a recently published procedure[51] based on the earlier experiments of Sau and Murphy[52] according to a two-step approach composed of a seeding process and a growth process. The seed solution was prepared by adding an ice-cold $NaBH_4$ solution (0.42 mL, 10 mM) into an aqueous solution composed of a mixture of $HAuCl_4$ (92 μL, 10 mM) and CTAB (7 mL, 100 mM). This seed solution was kept at 25 °C for 2 h to decompose excess borohydride before use. The growth solution was prepared by the successive addition of three aqueous solutions: CTAB (9 mL, 22 mM), $HAuCl_4$ (0.250 mL, 10 mM) and ascorbic acid (3 mL, 38 mM). Next, 20 μL of a water-diluted seed solution (1:50) was injected into the growth solution. The resultant solution was allowed to sit overnight at 25 °C. Concentrated solutions of nanocubes were obtained by centrifugation at 4500 rpm for 15 min, twice, and redispersion in a suitable amount of water. A few microliters of these concentrated solutions were dropcast on carbon-coated copper grids and indium tin oxide substrates for TEM and SEM measurements, respectively.

Chemicals. Cetyltrimethylammonium bromide (CTAB ≥ 98%), chloroauric acid ($HAuCl_4 \cdot 3H_2O$), sodium borohydride ($NaBH_4$, 99%), and ascorbic acid (99%) were purchased from Sigma and used as received. Deionized water was used for all experiments and dilutions.

Instrumentation. UV–Visible extinction spectra in solution were recorded with a 1 cm cell on a Jasco V-570 spectrophotometer. Transmission electron microscopy (TEM) observations were made using a Philips CM12 microscope operating at 120 kV.

Experimental Procedure. The azo dye molecule-containing polymer consists of pseudostilbene molecules, disperse red 1 (DR1), grafted as a side chain to polymethylmethacrylate (PMMA) in a 30% molar ratio (PMMA-DR1). PMMA-DR1 is dissolved in 1,1,2-trichloroethane and spin-coated onto the GNCs immobilized with electrostatic forces on an indium tin oxide (ITO) substrate.

AFM measurements showed that the polymer film is 40 nm thick on the substrate and about 10 nm thick above the cubes, allowing for characterization of the extremely confined near-field at the GNC surface. This point enables additional, novel imaging capabilities over previous (*e.g.*, ref 46) studies. Furthermore, the first use of a differential AFM imaging system with the photochemical imaging method allows one to get high contrast near-field optical images in the absence of any far-field background. The surface topology of the PMMA-DR1 polymer film can distort in the presence of light with a wavelength coinciding with the absorption maximum of the azobenzene chromophores.

Irradiation of the sample was performed at normal incidence for about 5 min with a *Z* propagating plane wave (λ = 530 nm) at a power density of 80 mW/cm^2 (Figure 1d). On the basis of Figure 1b, the electromagnetic excitation of the GNCs is somewhat to the blue of the dipolar resonance. The incident polarization state is linear and parallel to the *Y* axis and is kept constant. As illustrated in Figure 1a, the cubes have random in-plane orientation on the substrate, which enables a complete polarization study by considering several isolated GNCs that are oriented differently relative to the incident polarization. After exposure, the optically induced topography is analyzed by AFM.

Conflict of Interest: The authors declare no competing financial interest.

Acknowledgment. This work was supported by the Partner University Funds program (PUF2010). M.D. and G.C.S. were supported by the NSF MRSEC grant (DMR-1121262). Use of the Center for Nanoscale Materials (S.K.G., G.P.W.) was supported by the U.S. Department of Energy, Office of Science, Office of Basic Energy Sciences, under Contract No. DE-AC02-06CH11357. We thank the TEM team platform, DSV, CEA-Saclay. This work was also supported by the European community FEDER fund and the Region Champagne-Ardenne: Grants HYNOV and NANO'MAT (www.nanomat.eu).

Supporting Information Available: Additional experimental details and figures. This material is available free of charge *via* the Internet at http://pubs.acs.org.

REFERENCES AND NOTES

1. Sau, T. K.; Rogach, A. L.; Jäckel, F.; Klar, T. A.; Feldmann, J. Properties and Applications of Colloidal Nonspherical Noble Metal Nanoparticles. *Adv. Mater.* **2010**, *22*, 1805–1825.
2. Noguez, C. Surface Plasmons on Metal Nanoparticles: The Influence of Shape and Physical Environment. *J. Phys. Chem. C* **2007**, *111*, 3806–3819.
3. Lin, S. X.; Wong, C. Y.; Pun, E. Y. B.; Song, F. The Role of Metal Film Electron Density in a Surface Plasmon Polariton Assisted Light Emitter. *Nanotechnology* **2010**, *21*, 055203–055207.
4. Teo, S. L.; Lin, V. K.; Marty, R.; Large, N.; Llado, E. A.; Arbouet, A.; Girard, C.; Aizpurua, J.; Tripathy, S.; Mlayah, A. Gold Nanoring Trimers: A Versatile Structure for Infrared Sensing. *Opt. Express* **2010**, *18*, 22271–22282.
5. Polemi, A.; Wells, S.; Lavrik, N. V.; Sepaniak, M. J.; Shuford, K. Dispersions Characteristics in Disk-on-Pillar Array Nanostructures for Surface-Enhanced Raman Spectroscopy. *J. Phys. Chem. C* **2011**, *115*, 13624–13629.
6. Jain, P. K.; El-Sayed, M. A. Noble Metal Nanoparticles: Effect of Medium for Enhanced Nanosensing. *Nano Lett.* **2008**, *8*, 4347–4352.
7. Aubry, A.; Lei, D. Y.; Fernandez-Domínguez, A. I.; Sonnefraud, Y.; Maier, S. A.; Pendry, J. B. Plasmonic Light-Harvesting Devices over the Whole Visible Spectrum. *Nano Lett.* **2010**, *10*, 2574–2579.
8. Bergman, D. J.; Stockman, M. I. Surface Plasmon Amplification by Stimulated Emission of Radiation: Quantum Generation of Coherent Surface Plasmons in Nanosystems. *Phys. Rev. Lett.* **2003**, *90*, 027402–027405.
9. Srituravanich, W.; Pan, L.; Wang, Y.; Sun, C.; Bogy, D. B.; Zhang, X. Flying Plasmonic Lens in the Near Field for High-Speed Nanolithography. *Nat. Nanotechnol.* **2008**, *3*, 733–737.
10. Kawata, S.; Inouye, Y.; Verma, P. Plasmonics for Near-Field Nano-imaging and Superlensing. *Nat. Photonics.* **2009**, *3*, 388–394.
11. Kim, D. S.; Heo, J.; Ahn, S. H.; Han, S. W.; Yun, W. S.; Kim, Z. H. Real-Space Mapping of the Strongly Coupled Plasmons of Nanoparticles Dimers. *Nano Lett.* **2009**, *9*, 3619–3625.
12. Deeb, C.; Ecoffet, C.; Bachelot, R.; Plain, J.; Bouhelier, A.; Soppera, O. Plasmon-Based Free-Radical Photopolymerization: Effect of Diffusion on Nanolithography Processes. *J. Am. Chem. Soc.* **2011**, *113*, 10535–10542.
13. Sarid, D.; Callener, W. *Modern Introduction to Surface Plasmons: Theory, Mathematica Modeling, and Applications*; Cambridge University Press: Cambridge, 2010.

14. Valev, V. K.; Silhanek, A. V.; Jeyaram, Y.; Denkova, D.; DeClercq, B.; Petkov, V. V.; Zheng, X.; Volskiy, V.; Gillijns, W.; Vandenbosch, G. A. E.; *et al.* Hotspot Decorations Map Plasmonic with the Resolution of Scanning Probes Techniques. *Phys. Rev. Lett.* **2011**, *106*, 226803–226806.
15. Nelayah, J.; Kociak, M.; Stéphan, O.; García de Abajo, F. J.; Tencé, M.; Henrard, L.; Taverna, D.; Pastoriza-Santos, I.; Liz-Marzán, L. M.; Colliex, C. Mapping Surface Plasmon on a Single Metallic Nanoparticle. *Nat. Phys.* **2007**, *3*, 348–353.
16. Dormüller, J.; Vogelgesang, R.; Weitz, R. T.; Rockstuhl, C.; Etrich, C.; Pertsch, T.; Lederer, F.; Kern, K. Fabry−Perot Resonances in One-Dimensional Plasmonic Nanostructures. *Nano Lett.* **2009**, *9*, 2372–2377.
17. Vesseur, E. J. K.; de Waele, R.; Kuttge, M.; Polman, A. Direct Observation of Plasmonic Modes in Au Nanowires Using High-Resolution Cathodoluminescence Spectroscopy. *Nano Lett.* **2007**, *7*, 2843–2846.
18. Kubo, A.; Jung, Y. S.; Kim, H. K.; Petek, P. Femtosecond Microscopy of Localized and Propagating Surface Plasmons in Silver Gratings. *J. Phys. B: Atom. Mol. Opt. Phys.* **2007**, *40*, S259–S272.
19. Bouhelier, A.; Beversluis, M. R.; Novotny, L. Characterization of Nanoplasmonic Structures by Locally Excited Photoluminescence. *Appl. Phys. Lett.* **2003**, *83*, 5041–5043.
20. Gates, B. D.; Xu, Q.; Stewart, M.; Ryan, D.; Willson, C. G.; Whitesides, G. M. New Approaches to Nanofabrication: Molding, Printing, and Other Techniques. *Chem. Rev.* **2005**, *105*, 1171–1196.
21. Enüstün, B. V.; Turkevich, J. Coagulation of Colloidal Gold. *J. Am. Chem. Soc.* **1963**, *85*, 3317–3328.
22. Turkevich, J. Colloidal Gold. Part I: Historical and Preparative Aspects, Morphology and Structure. *Gold Bull.* **1985**, *18*, 86–91.
23. Frens, G. Controlled Nucleation for the Regulation of the Particle Size in Monodisperse Gold Suspensions. *Nat. Phys. Sci.* **1973**, *241*, 20–22.
24. Nagpal, P.; Lindquist, N. C.; Oh, S. H.; Norris, D. J. Ultrasmooth Patterned Metals for Plasmonics and Metamaterials. *Science* **2009**, *325*, 594–597.
25. Wells, O. C. *Introduction to Electron Beam Technology*; Bakish, R., Eds.; John Wiley & Sons, Inc.: New York, 1962.
26. Xia, Y.; Kim, E.; Zhao, X. M.; Rogers, J. A.; Prentiss, M.; Whitesides, G. M. Complex Optical Surfaces Formed by Replica Molding against Elastomeric Masters. *Science* **1996**, *273*, 347–349.
27. Chou, S. Y.; Krauss, P. R.; Renstrom, P. J. Imprint Lithography with 25-Nanometer Resolution. *Science* **1996**, *272*, 85–87.
28. Xia, Y.; Whitesides, G. M. Soft Lithography. *Annu. Rev. Mater. Sci.* **1998**, *28*, 153–184.
29. Eigler, D. M.; Schweizer, E. K. Positioning Single Atoms with a Scanning Tunneling Microscope. *Nature* **1990**, *344*, 524–526.
30. Aizenberg, J.; Black, A. J.; Whitesides, G. M. Control of Crystal Nucleation by Patterned Self Assembled Monolayers. *Nature* **1999**, *398*, 495–498.
31. Zach, M. P.; Ng, K. H.; Penner, R. M. Molybdenum Nanowires by Electrodeposition. *Science* **2000**, *290*, 2120–2123.
32. Whitesides, G. M.; Mathias, J. P.; Seto, C. T. Molecular Self-Assembly and Nanochemistry: A Chemical Strategy for the Synthesis of Nanostructures. *Science* **1991**, *254*, 1312–1319.
33. Sisco, P. N.; Murphy, C. J. Surface-Coverage Dependence of Surface-Enhanced Raman Scattering from Gold Nanocubes on Self-Assembled Monolayers of Analyte. *J. Phys. Chem. A* **2009**, *113*, 3973–3978.
34. Wu, X.; Ming, T.; Wang, X.; Wang, P.; Wang, J.; Chen, J. High-Photoluminescence-Yield Gold Nanocubes: For Cell Imaging and Photothermal Therapy. *ACS Nano* **2010**, *4*, 113–120.
35. Yang, Z.; Chiang, C.-K.; Chang, H.-T. Synthesis of Fluorescent and Photovoltaic Cu_2O Nanocubes. *Nanotechnology* **2008**, *19*, 025604:1–025604:7.
36. Sherry, L. J.; Chang, S. H.; Schatz, G. C.; Van Duyne, R. P.; Wiley, B. J.; Xia, Y. N. Localized Surface Plasmon Resonance Spectroscopy of Single Silver Nanocubes. *Nano Lett.* **2005**, *5*, 2034–2038.
37. Zhang, S.; Bao, K.; Halas, N. J.; Xu, H.; Nordlander, P. Substrate-Induced Fano Resonances of a Plasmonic Nanocube: A Route to Increased-Sensitivity Localized Surface Plasmon Resonance Sensors Revealed. *Nano Lett.* **2011**, *11*, 1657–1663.
38. McMahon, J.-M.; Wang, Y.; Sherry, L. J.; Van Duyne, R.-P.; Marks, L.-D.; Gray, S.-K.; Schatz, G.-C. Correlating the Structure, Optical Spectra, and Electrodynamics of Single Silver Nanocubes. *J. Phys. Chem.C* **2009**, *113*, 2731–2735.
39. Ringe, E.; McMahon, J.-M.; Sohn, K.; Cobley, C.; Xia, Y.; Huang, J.; Schatz, G.-C.; Marks, L.-D.; Van Duyne, R.-P. Unraveling the Effects of Size, Composition, and Substrate on the Localized Surface Plasmon Resonance Frequencies of Gold and Silver Nanocubes: A Systematic Single-Particle Approach. *J. Phys. Chem. C* **2010**, *114*, 12511–12516.
40. Juan, M. L.; Plain, J.; Bachelot, R.; Royer, P.; Gray, S. K.; Wiederrecht, G. P. Multiscale Model for Photoinduced Molecular Motion in Azo Polymers. *ACS Nano* **2009**, *3*, 1573–1579.
41. Juan, M. L.; Plain, J.; Bachelot, R.; Royer, P.; Gray, S. K.; Wiederrecht, G. P. Self-Consistent Model of Light-Induced Molecular Motion around Metallic Nanostructures. *J. Phys. Chem. Lett.* **2010**, *1*, 2228–2232.
42. Moskovits, M. Imaging: Spot the Hot Spot. *Nature* **2011**, *469*, 307–308.
43. Born, M.; Wolf., E. *Principles of Optics*; Cambridge University Press: Cambridge, 1999.
44. Jana, N. R.; Gearheart, L.; Murphy, C. J. Seed-Mediated Growth Approach for Shape-Controlled Synthesis of Spheroidal and Rod-like Gold Nanoparticles Using a Surfactant Template. *Adv. Mater.* **2001**, *13*, 1389–1393.
45. Sau, T. K.; Rogach, A. L. Nanospherical Noble Metal Nanoparticles: Colloid-Chemical Synthesis and Morphology Control. *Adv. Mater.* **2010**, *22*, 1781–1804.
46. Hubert, C.; Bachelot, R.; Plain, J.; Kostcheev, S.; Lerondel, G.; Juan, M.; Royer, P.; Zou, S.; Schatz, G. C.; Wiederrecht, G. P.; *et al.* Near-Field Polarization Effects in Molecular-Motion-Induced Photochemical Imaging. *J. Phys. Chem. C* **2008**, *112*, 4111–4116.
47. Juan, M.; Plain, J.; Bachelot, R.; Vial, A.; Royer, P.; Gray, S. K.; Montgomery, J.; Wiederrecht, G. P. Plasmonic Electromagnetic Hot Spots Temporally Addressed by Photoinduced Molecular Displacement. *Phys. Chem A* **2009**, *113*, 4647–4651.
48. Galarreta, B. C.; Rupar, I.; Young, A.; Lagugné-Labarthet, F. Mapping Hot-Spots in Hexagonal Arrays of Metallic Nanotriangles with Azobenzene Polymer Thin Films. *J. Phys. Chem. C* **2011**, *115*, 15318–15323.
49. Gilbert, Y.; Bachelot, R.; Royer, P.; Bouhelier, A.; Wiederrecht, G. P.; Novotny, L. Longitudinal Anisotropy of the Photoinduced Molecular Migration in Azobenzene Polymer Films. *Opt. Lett.* **2006**, *31*, 613–615.
50. Bachelot, R.; Gleyzes, P.; Boccara, A. C. Near-Field Optical Microscope Based on Local Perturbation of a Diffraction Spot. *Opt. Lett.* **1995**, *20*, 1924–1926.
51. Yu, Y.; Zhang, Q.; Lu, X.; Lee, J. Y. Seed Mediated Synthesis of Monodisperse Concave Trisoctahedral Gold Nanocrystals with Controllable Sizes. *J. Phys. Chem. C* **2010**, *114*, 11119.
52. Sau, T. K.; Murphy, C. J. Room Temperature High Yield Synthesis of Multiple Shapes of Gold Nanoparticles in Aqueous Solution. *J. Am. Chem. Soc.* **2004**, *126*, 8648.